Nuclear Science and Techniques (2024) 35:193
https://doi.org/10.1007/s41365-024-01540-z

Effect of long-term thermal exposure on microstructure of laser-welded UNS N10003 alloy

Kun Yu[1] · **Yuan Zhang**[1] · **Xiao-Dan Yuan**[1] · **Li-Bin Zhao**[2] · **Zhi-Jun Li**[1]

Received: 20 December 2023 / Revised: 4 February 2024 / Accepted: 7 March 2024 / Published online: 10 October 2024

Abstract

The evolution of the microstructure and tensile rupture mechanism of laser welds in UNS N10003 alloy exposed to 700 °C are investigated. Fine M_6C carbides precipitate around the primary eutectic M_6C-γ carbides in the fusion zone after 100 h of exposure. During long-term thermal exposure, the size of the fine M_6C carbides increased. The eutectic M_6C-γ carbides in the as-welded fusion zone transformed into spherical M_6C carbides as the exposure time extends to 10000 h. Additionally, the spherical M_6C particles exhibit size coarsening with increasing exposure time. The tensile properties of the welded joints are not adversely affected by the evolution of eutectic M_6C-γ carbides and the coarsening of M_6C carbides.

Keywords UNS N10003 alloy · Laser welding · M_6C · Long-term thermal exposure

1 Introduction

Molten salt reactors are among the most promising fourth-generation nuclear reactors owing to their inherent merits, such as high safety, minimization of nuclear waste, and high power generation efficiency [1–6]. The UNS N10003 alloy, which is named the GH3535 alloy in China, was designed for thorium molten salt reactors (TMSRs) owing to its excellent mechanical properties and corrosion resistance [7–12].

The UNS N10003 alloy, which was selected as the primary structural material for TMSRs, has been used at 700 °C for more than 20 years. Meanwhile, studies showed that some nickel-based alloys exhibit degraded mechanical properties after long-term aging [13, 14]. This is a key issue affecting reactor service safety. Hence, the microstructure and property stability of the alloy are major concerns for designers.

Based on previous studies [15–17], $M_{12}C$ carbides precipitated at the grain boundaries in GH3535 alloy during long-term thermal exposure at 700 °C. The precipitation of $M_{12}C$ carbides can affect the alloy ductility with increasing thermal-exposure time. Additionally, the precipitation of $M_{12}C$ carbide was shown to improve the creep properties of the alloy. However, studies pertaining to the effect of thermal exposure on microstructures are primarily focused on the base metal of the UNS N10003 alloy; its effect on welded joints has not been reported. Welding is an essential component of manufacturing technology, particularly in the nuclear industry. The failure of components is typically caused by the failure of the welded joint due to the inhomogeneity of the microstructure and the properties of the welded joint. Hence, the welded joints of UNS N10003/GH3535 alloy must be investigated comprehensively to ensure the safety of TMSRs. Previously, researchers [18–22] have focused on the evolution of the microstructure and mechanical properties of UNS N10003 joints welded via gas tungsten arc welding (GTAW). They discovered that eutectic carbides precipitated in the fusion zone (FZ) and eutectic carbides in the heat-affected zone (HAZ) transformed from the original spherical carbides of the base metal. Additionally, the post-weld heat treatment (PWHT) of the welded joint was investigated. The result showed that the eutectic M_6C carbides in the FZ and

---

This study was supported by the Technology Star of Shanghai Institute of Applied Physics, Chinese Academy of Sciences (No. E2551130) and the Youth Innovation Promotion Association, Chinese Academy of Sciences (No. E2292202).

✉ Li-Bin Zhao
zhlbhit@126.com

✉ Zhi-Jun Li
lizhijun@sinap.ac.cn

[1] Shanghai Institute of Applied Physics, Chinese Academy of Sciences, Shanghai 201800, China

[2] Nuclear and Radiation Safety Center, Beijing 100082, China

Table 1 Chemical composition of UNS N10003 alloy (wt.%)

Ni	Mo	Cr	Fe	Mn	Si	Al	C	B	S	P
Bal	17.20	6.95	4.06	0.628	0.43	0.07	0.054	0.0008	0.001	0.005

Table 2 Laser-beam welding parameters

Peak power per pulse (kw)	Pulse frequency (Hz)	Duty cycle of laser (%)	Welding speed (m/min)	Defocus amount (mm)	Shielding gas	Top shielding gas flow (L/min)	Back shielding gas flow (L/min)
2.8	35	60	0.8	−2	Ar	20	15

HAZ transformed into spheres after solid-solution treatment at 1100 °C [23]. In our previous study [24, 25], we investigated the microstructure and tensile properties of laser-welded joints in GH3535 alloy under as-welded and PWHT conditions at 871 °C for 6 h. The precipitates significantly affected the mechanical properties. Although some studies have focused on welded joints in UNSN10003/GH3535, they did not systematically investigate the microstructure evolution and rupture mechanism of the welded joints after long-term thermal exposure.

In this study, the effects of long-term thermal exposure at 700 °C on the microstructure and tensile rupture mechanism of laser welds are investigated. The evolution of the grain structure, size, and morphology of carbides is characterized, in addition to the tensile rupture morphologies of welded joints. Subsequently, the precipitate stability and tensile rupture mechanism of the laser welds are discussed comprehensively.

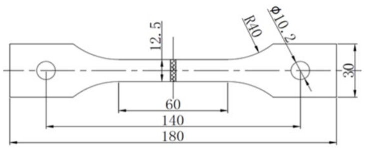

Fig. 1 Specimen for tensile test

2 Materials and experimental methods

UNS N10003 alloy was provided under solution treatment conditions by Fushun Special Steel Shares Co., Ltd.. It is a solution-strengthened nickel-based alloy comprising an austenite γ phase and M_6C carbides [26, 27]. The UNS N10003 alloy plate was segmented into small plates measuring 300 mm × 100 mm × 4 mm. The chemical composition of the UNS N10003 alloy is listed in Table 1.

Two plates of UNS N10003 alloy were ground via sandblasting to remove the surface oxide and then cleaned using acetone prior to welding. Two plates with I-grooves were fixed in a butt configuration. Welding experiments were performed using an IPG YLS.10000 fiber laser. A laser beam with a wavelength of 1.06 µm was transmitted to the laser welding head via an optical fiber with a core diameter of 200 µm. The laser beam was focused onto a spot with a diameter of 0.26 µm using a mirror with a focal length of 200 mm. The laser welding head was mounted on a six-axis KUKA robot. The process parameters for laser welding without any filler metal are listed in Table 2. The welding parameters were optimized based on the radiographic testing results of weldments.

The weldments were cut into small specimens. Subsequently, the specimens were exposed to a furnace of air atmosphere at 700 °C for various durations up to 10000 h. Each specimen was removed from the furnace at a specified time and then allowed to cool naturally.

The thermally exposed welded joints were segmented to form specimens. Cross sections of the welded joints for microstructure observation were mounted in epoxy resin, ground with SiC paper, and polished with 0.05 µm alumina paste for 2 min. A Zeiss M2m optical microscope (OM) system and a Zeiss Merlin Compact scanning electron microscope (SEM) system equipped with electron backscatter diffraction (EBSD) were used to observe the morphology of the microstructure. The OM and SEM specimens were etched using a solution comprising 3 g of $CuSO_4$ and 80 mL of HCl for 30 s. The EBSD specimens were polished using a vibratory finishing machine for 1 h without solution etching. A Tecnai G2 F20 S-TWIN TEM equipped with an energy-dispersive X-ray system was used to analyze the precipitates. The TEM specimens were punched into disks with a diameter of 3 mm and a thickness of 100 µm. The disks were electrochemically treated using a twin-jet electropolishing device with a solution comprising 90% ethanol and 10% perchloric acid.

A Zwick/Roell Z100 universal material machine was used to test the tensile properties of the welded joints at 700 °C. The tensile specimens measuring 50 mm in gauge length are shown in Fig. 1.

3 Results and discussion

3.1 Grain evolution of welded joint

Figure 2a–c shows the microstructures of the as-welded joints. Figure 2a shows the macromorphology of the joints. As shown, the central region is the FZ. Some large black precipitates (indicated by red arrows) were observed in the HAZ near the fusion line. Figure 2b clearly shows the morphology of the eutectic M_6C-γ carbides near the fusion line, which was identified in our previous study [25]. The eutectic M_6C-γ carbides was transformed from the spherical M_6C carbides of the base metal (BM) via the thermal welding. Figure 2c shows the microstructure of the BM, which is composed of the equiaxial austenite phase and the M_6C carbides distributed in the grain boundaries and internal grains [26, 27].

Figure 2d shows the microstructure of the as-welded FZ. The FZ was composed of columnar crystals and fine cells. The solidification grain boundary (SGB), which distinguishes differently oriented subcrystals, could not be observed easily. Figure 2e and f shows that the microstructure of the FZ was adversely affected by thermal exposure for 100 h and 10000 h at 700 °C, respectively. Additionally, numerous black phases and SGBs were indicated.

To clearly observe the grain morphology, we performed an EBSD experiment. Figure 3 shows the grain morphology of the as-welded joint and the joint exposed thermally for 10000 h at 700 °C. As shown, the microstructure of the FZ exposed thermally for 10000 h was composed of columnar crystals. This is attributable to the non-migration or slow migration of the grain boundaries. Figure 4 shows a grain size comparison of the FZ, HAZ, and BM before and after thermal exposure using EBSD and the Tango software. As shown, the average grain sizes of the FZ, HAZ, and BM were 57.1 μm, 47.5 μm, and 48.7 μm under the as-welded condition, respectively. After thermal exposure for 10000 h at 700 °C, the average grain sizes of the FZ, HAZ, and BM were 60.6 μm, 52.1 μm, and 50.3 μm, respectively. A certain degree of grain boundary migration resulted in slight grain coarsening. This suggests that the microstructure was extremely stable, which is attributable to two reasons. First, N10003 alloy contains 72 wt.% Ni, which endows excellent stability to the austenite microstructure. Second, the grain boundaries of the joint precipitated secondary phases,

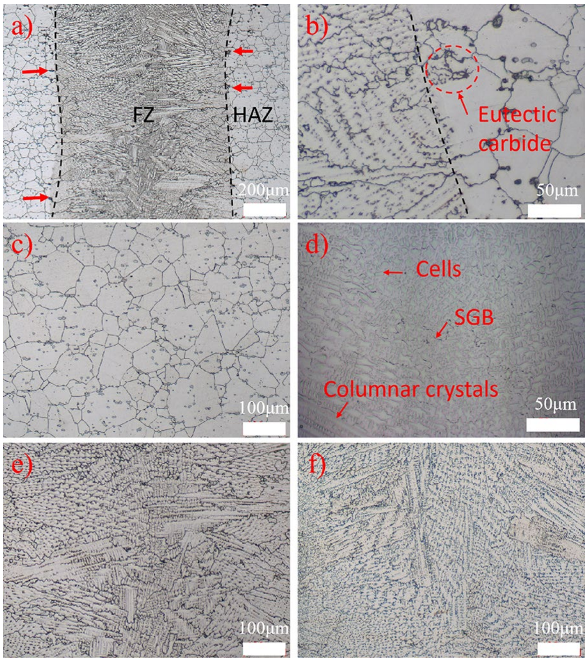

Fig. 2 Typical microstructure of joint. **a** Morphology of joint; **b** HAZ; **c** BM; **d** as-welded FZ; **e** FZ thermally exposed for 700 °C /100 h; **f** FZ thermally exposed for 700 °C/10000 h

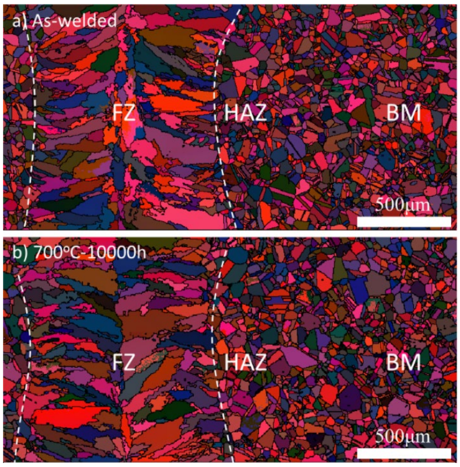

Fig. 3 (Color online) Grain morphology of as-welded and thermally exposed joint via EBSD

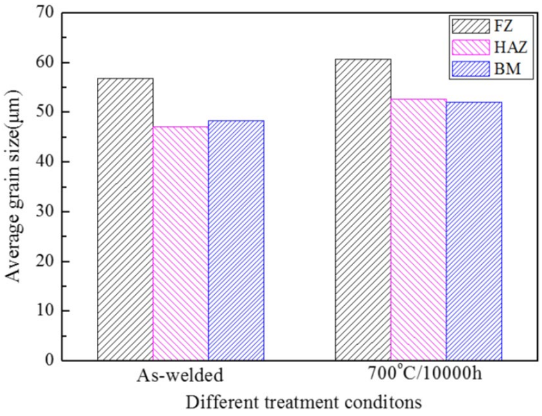

Fig. 4 Average grain sizes of as-welded and thermally exposed joint

which exerted a nailing effect on the grain boundaries during thermal exposure. Even when the atoms were thermally activated conditions, atomic diffusion, i.e., the migration of the grain boundary, did not occur readily.

3.2 Precipitate evolution of welded joint

3.2.1 FZ

We performed SEM to further investigate the effect of thermal exposure on the microstructure. Figure 5a shows the M_6C-γ carbides in the interdendritic region of the as-welded FZ [25]. Figure 5b shows the precipitate evolution after thermal exposure for 50 h at 700 °C. As shown, nanosized fine carbides precipitated near the primary M_6C-γ carbides. After thermal exposure for 100 h, the fine carbides near the primary M_6C-γ carbides enlarged to approximately 30 nm, as shown in Fig. 5c. Upon closer inspection, these fine carbides precipitated in the interdendritic region. After thermal exposure for 1000 h, the γ region of the eutectic M_6C-γ carbides decreased and was gradually replaced by carbides, as shown in Fig. 5d. This occurred owing to the ease of atomic diffusion, as the solute atoms are activated by high temperatures; thus, the system seeks to lower the Gibbs free energy. The primary carbides were rod-shaped staggered structures, in which the surface areas between the γ and M_6C phases were larger, i.e., the surface energy is higher compared with those of other surface areas. Atomic diffusion causes the carbide shape to change at high temperatures, so that the surface areas between phases are reduced; that is, the surface energy can be reduced. Thus, the Gibbs free energy of the system can be reduced. Except for the change in the appearance of the eutectic carbide, the size of nanoscale precipitates near the eutectic carbides increased to approximately 0.5 µm. After thermal exposure for 3000 h, the γ phases of the eutectic carbides disappeared, and the carbides remained spherical, as shown in Fig. 5e. After thermal exposure for 10000 h, all the carbides remained spherical, and the fine precipitates near the carbides enlarged, as shown in Fig. 5f.

The phase structures of the precipitates were analyzed using TEM, as shown in Fig. 6. The primary and fine secondary precipitates after thermal exposure for 100 h were analyzed. The main elements in the fine secondary precipitates were 5.18% Si, 8.15% Cr, 0.23% Fe, 31.06% Ni, and 54.99% Mo. The structure of fine secondary precipitate was M_6C carbide, which is a face-centered cubic (FCC) structure with lattice parameters measuring 11.15 Å, as shown in Fig. 6a and b. The main elements in the primary precipitate were 4.48% Si, 8.84% Cr, 0.15% Fe, 28.92% Ni, and 58.09% Mo. The structure of the primary precipitate was M_6C carbide, which is an FCC structure with lattice parameters measuring 11.05 Å, as shown in Fig. 6c and d. As shown, the structure of the eutectic carbide remained unchanged.

The primary and secondary precipitates after thermal exposure for 10000 h were analyzed using TEM, as shown in Fig. 7. The primary elements in the secondary precipitate were 4.00% Si, 1.05% Cr, 28.07% Ni, and 66.86% Mo. The structure of the secondary precipitates was identified as M_6C carbide, which is an FCC structure with lattice parameters measuring 10.96 Å, as shown in Fig. 7a and b. The main elements in the primary precipitate were 2.08% Si, 0.74% Cr, 25.50% Ni, and 71.67% Mo. The structure of the primary precipitate was identified as M_6C carbide, which is an

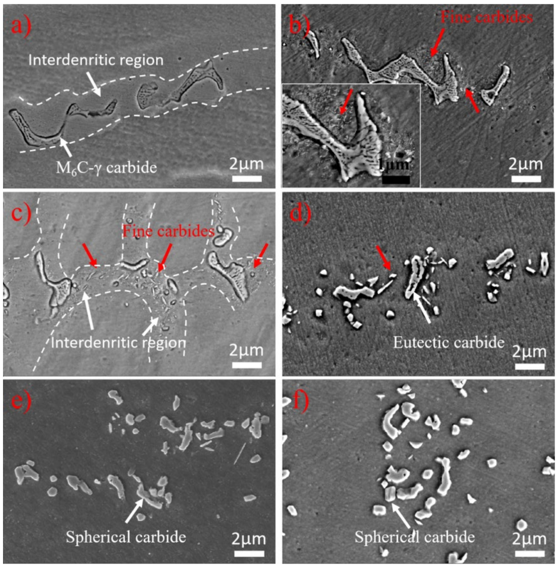

Fig. 5 Evolution of carbides in FZ under different thermal-exposure times: **a** as-welded; **b** 50 h; **c** 100 h; **d** 1000 h; **e** 3000 h; **f** 10000 h

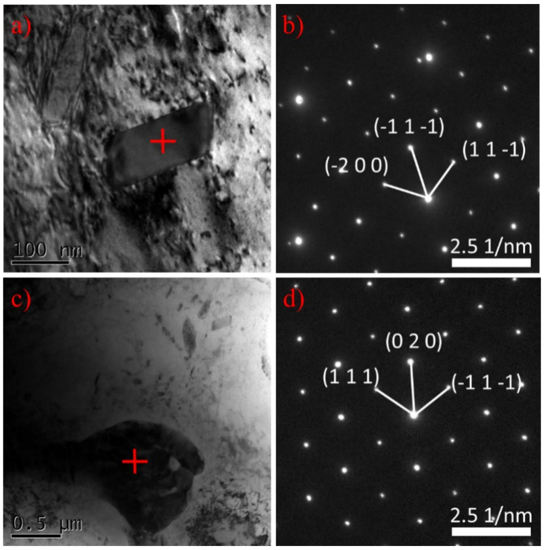

Fig. 6 TEM analysis of precipitates treated at 700 °C for 100 h: **a** and **b** secondary precipitate **c** and **d** primary precipitate

FCC structure with lattice parameters measuring 10.99 Å, as shown in Fig. 7c and d. The structure of the primary carbide remained unchanged owing to the excellent high-temperature stability of M_6C. The microstructural evolution under different process conditions is shown in Table 3. As shown, M_6C-γ and M_2C carbides precipitated in the FZ of GTAW under the as-welded condition. Subsequently, the M_2C carbides were converted into M_6C carbides via PWHT at temperatures above 950 °C [18, 21, 23]. In other studies [19, 20], the precipitates were MoC carbides welded viva GTAW. Li et al. analyzed the precipitates in GH3535 alloy with different Si contents [28]. When the Si content of the alloy was 0.051 wt.% and 0.188 wt.%, M_2C and M_6C carbides were precipitated from the cast GH3535 alloy, respectively. Additionally, M_2C was gradually replaced by M_6C after thermal exposure for 500 h at 750 °C. However, when the Si content was 0.562 wt.% and 1.01 wt.%, only M_6C carbide was present in the alloy. This is because an increase in the Si content reduces the Gibbs free energy of M_6C; thus, the nucleation rate of M_6C is higher. However, Si does not significantly affect the nucleation of M_2C. Thus, the M_6C carbide offers the advantage of high nucleation. During thermal exposure, Mo and C in M_2C diffuse to the surrounding substrate, thus facilitating their conversion to M_6C. In this study, the Si content of the alloy was 0.43 wt.%, which signifies an alloy of high Si content. The nucleation rate of M_6C is higher than that of M_2C. Additionally, element segregation was inhibited by the high solidification rate of the laser melting pool, thus resulting in Mo and C segregation and failure to attain the conditions for the formation of M_2C. Therefore, M_2C carbides were not present in the laser weld under the as-welded/PWHT and thermal-exposure conditions [24, 25, 27].

Meanwhile, the coarsening of carbides in the SGB under different thermal-exposure times showed a similar behavior to that of the interior grains shown in Fig. 8. In our previous studies, we primarily focused on the interdendritic region when examining the segregation of the FZ [25, 27]. In this study, we discovered that the SGB was in the interdendritic region, as shown in Fig. 8a. After thermal exposure, carbides precipitate at the SGB because of segregation and vacancy defects [24]. The carbides increased in size and then stabilized as thermal exposure progresses.

Table 3 Different microstructural evolutions under different process conditions

Process conditions	Primary carbide type		Secondary carbide type		Literatures
Laser welding	As-welded	M_6C-γ	Aging	M_6C	This paper
			PWHT	M_6C	[24, 25, 27]
GTAW	As-welded	M_6C-γ/M_2C	PWHT	M_6C/M_2C	[18, 21, 23]
	As-welded	MoC	/		[19, 20]
Base metal	High Si	M_6C	Aging	$M_6C/M_{12}C$	[16]
	Low Si	M_6C/M_2C	Aging	M_6C	[28]

SEM and the IPP software were used to analyze the size of the carbides. More than 20 carbides zoomed in by 20000X were analyzed using the IPP software to calculate the area and convert it into a diameter. The change in the particle size of the secondary precipitates around the primary carbides is indicated by the red line in Fig. 9. The area of the carbides was calculated using the IPP software, and the area of the graph was divided to obtain the area score from three SEM graphs zoomed in by 5000X. The change in the area score of the FZ is indicated by the blue line in Fig. 9. The size of the primary carbides did not increase significantly, whereas the growth of the secondary carbides was evident; therefore, the

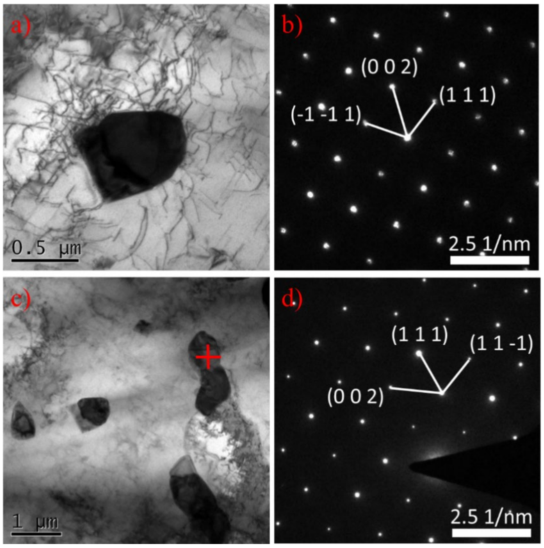

Fig. 7 TEM analysis of precipitates treated at 700 °C for 10000 h: **a** and **b** secondary precipitate; **c** and **d** primary precipitate

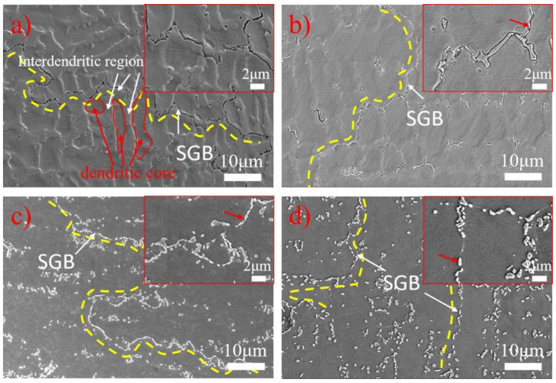

Fig. 8 Coarsening of carbides in SGB under different thermal-exposure times: **a** as-welded; **b** 100 h; **c** 3000 h; **d** 10000 h

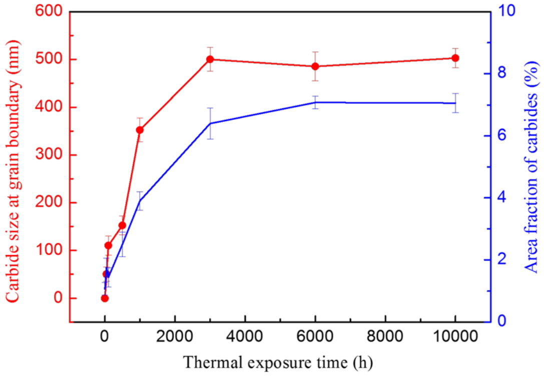

Fig. 9 Evolution of secondary precipitate sizes and area fraction of carbides

area score of the total carbides increased continuously. The size of the carbides increased rapidly at approximately 0.35 nm/h within 1000 h of thermal exposure owing to the high degree of element segregation, which caused the carbides to grow rapidly. During thermal exposure from 1000 h to 3000 h, the carbides grew gradually at approximately 0.075 nm/h. When the thermal-exposure time increased to 3000 h, the carbide content stabilized and carbide growth was no longer evident.

3.2.2 HAZ

Figure 10 shows the evolution of the eutectic M_6C-γ carbides under different thermal-exposure times. Figure 10a shows the morphology of the eutectic carbide. The transformation mechanism of eutectic carbides in GH3535 alloy has been investigated previously [22, 23, 25]. The spherical M_6C carbides in the BM were subjected to a temperature above 1300 °C in the welding thermal cycle, thus causing the spherical M_6C carbides to melt. As the temperature decreased, the carbides precipitate in a striped form and reacted with the surrounding γ substrate. The eutectic reaction process is expressed as γ+M_6C(p)→ γ+L→ γ+M_6C(e), where M_6C(p) is the spherical carbide in the BM and M_6C(e) is the eutectic carbide. After thermal exposure for 50 h at 700 °C, the morphology of the eutectic carbides remained unchanged, whereas fine secondary precipitates formed in the area surrounding the eutectic carbides, as shown by the red arrow in Fig. 10b. As the thermal-exposure time increased up to 1000 h, the size of the secondary precipitates increased, whereas the morphology of the eutectic carbides remained unchanged, as shown in Fig. 10c and d. After thermal exposure for 3000 h, the morphology of the eutectic carbides, which comprised bar and spherical carbides, changed (see Fig. 10e). After thermal exposure for 10000 h, the carbides were devoid of bar carbides, as all of them were converted into spherical carbides, as shown in Fig. 10f.

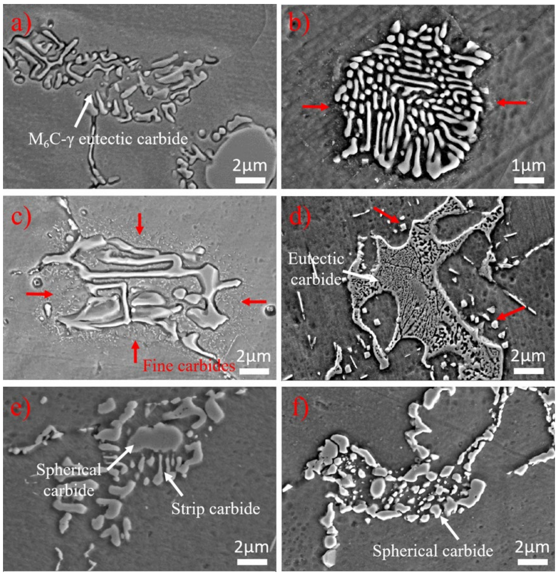

Fig. 10 Evolution of eutectic carbides in HAZ under different thermal-exposure times: **a** as-welded; **b** 50 h; **c** 100 h; **d** 1000 h; **e** 3000 h; **f** 10000 h

The evolution of the carbides from eutectic to spherical was governed by the Gibbs free energy of the system. The eutectic carbides were primarily composed of strip carbides under the as-welded condition. The carbides under thermal exposure enlarged owing to the thermal diffusion of atoms. The surface area of the carbides increased, which consequently increased the Gibbs free energy of the system and rendered the system unstable. At this point, the microstructure evolved to obtain a stable system energy. Hence, spherical carbides were formed because their surface areas were smaller than those of the strip carbides, which reduces the Gibbs free energy. Figure 11 shows the structure of the carbide in the HAZ after thermal exposure for 10000 h. Based on the results of selected electronic diffraction experiments, the carbide remained an M_6C carbide with an FCC structure and a lattice parameter of 10.92 Å. In summary, the M_6C carbide demonstrates excellent high-temperature stability and its shape is affected by changes in the free energy.

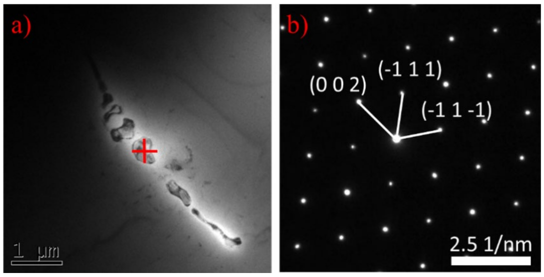

Fig. 11 TEM analysis of precipitates treated at 700 °C for 10000 h

3.2.3 BM

Figure 12 shows the microstructural evolution of the BM under different thermal-exposure times. No precipitates were observed at the grain boundaries, whereas large spherical M_6C carbides were observed in the interior grains in the case without thermal exposure, as shown in Fig. 12a. Figure 12b–e shows the morphology of the precipitates under thermal exposure for 50 h to 3000 h. The primary M_6C carbides did not change significantly as thermal exposure progressed. Meanwhile,, the secondary phases precipitated at the grain boundary and their size increased gradually over time. Figure 12f shows the morphology of the precipitates under thermal exposure for 10000 h. As shown, the secondary precipitates in the grain boundary enlarged and became more continuous. The size statistics of the secondary precipitates at the grain boundary (with error bars) for a series of thermal-exposure times were obtained using the IPP software, as shown in Fig. 13. As thermal exposure progressed, the secondary precipitates at the grain boundary enlarged continuously. When the thermal-exposure time reaches 10000 h, the secondary precipitates at the grain boundary measured 570 nm. The size of the precipitates increased rapidly at approximately 2 nm/h within 100 h of thermal exposure because of increased defects, such as empty positions at the grain boundary. The grain boundary can easily capture diffused solute elements, thus causing the precipitates to grow rapidly. During the thermal exposure from 100 h to 6000 h, the precipitates enlarged gradually at a relatively stable rate of approximately 0.06 nm/h. After 6000 h, the size of the precipitates stabilized. The structure of precipitates after thermal exposure has been systematically investigated [15, 16]. Using X-ray diffraction, TEM, and other material characterization methods, researchers discovered that the precipitates at the grain boundary were $M_{12}C$ with an FCC structure.

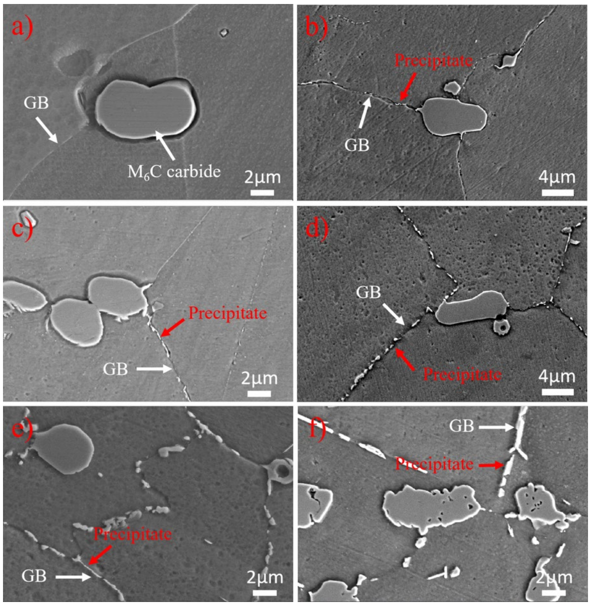

Fig. 12 Evolution of carbides in BM under different thermal-exposure times: **a** as-welded; **b** 50 h; **c** 100 h; **d** 1000 h; **e** 3000 h; **f** 10000 h

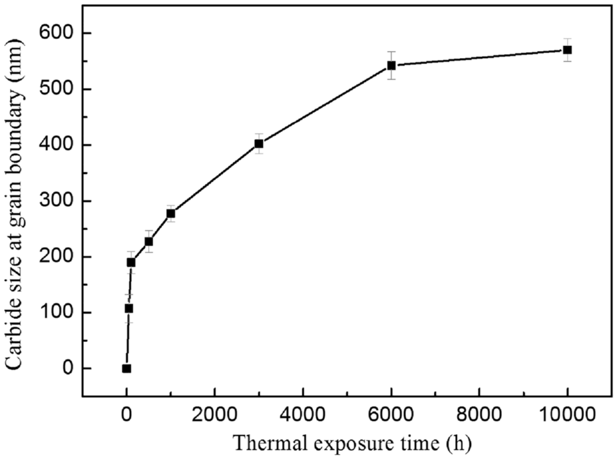

Fig. 13 Evolution of precipitate sizes in BM

3.3 Rupture mechanism of welded joints

To analyze the fracture behavior of the welded joint, the tensile fracture position of the welded joint was first analyzed. According to the statistics, the fracture locations of all tensile specimens were not in the FZ but in the BM near the FZ, as shown in Fig. 14. During the tensile process, the BM first yielded. The numerous carbides in the FZ exerted a nailing effect at the grain boundaries, thus preventing the slipping of dislocations and increasing the strength of the FZ. The strengthening mechanism can be explained using the Orowan strengthening theory [29]. When the secondary particles were larger and more rigid, the moving dislocation

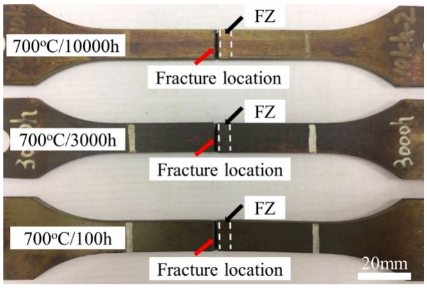

Fig. 14 (Color online) Tensile fracture location of joints under different thermal-exposure times

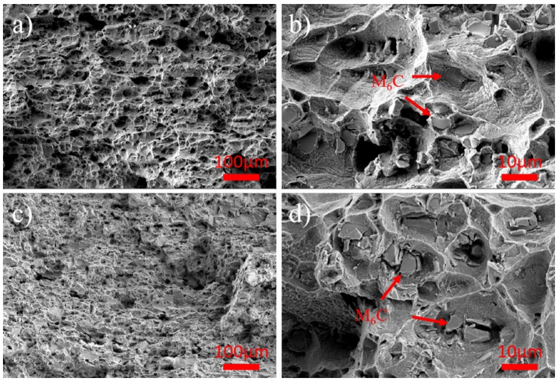

Fig. 15 Fracture morphology of joints subjected to tensile test: **a** and **b** as-welded; **c** and **d** 700/10000 h

could not easily cut through and bypass them, thus resulting in small dislocation rings around them.

During the tensile process, if no severe cracks or brittle phases are present in the FZ, then tensile deformation will first occur in the low-strength BM until fracture occurs. Tensile fracture occurred near the FZ, as shown in Fig. 14, as the latter was a region with both high and low strengths. During the deformation process, the strain in this region was particularly concentrated; thus, it was more susceptible to fracture [18]. After thermal exposure, although the secondary precipitates and primary carbides in the FZ enlarged, the size of the carbides was approximately 2 µm. The size and amount of the carbides affected the weld strengthening without resulting in tensile cracks derived from the carbides in the FZ. The size of the primary carbides in the BM reached 6 µm, as shown in Fig. 12. During the deformation process, the dislocation slip was primarily nailed and hindered by the precipitates at the grain boundary. As the tensile stress increased, cracks generated at the interface between the large M_6C and the matrix [15]. This region was located in high- and low-hardness phases, where dislocation piling and strain concentration occurred. The existence and evolution of the eutectic structure in the HAZ of the N10003 alloy did not result in the liquefaction and cracking of the grain boundaries, which were observed in other nickel-based alloys [30, 31].

Figure 15 shows the fracture morphology observed at 700 °C of the as-welded joint and joint exposed thermally for 10000 h. As shown, the fracture of the two joints contained numerous dimples featuring granular carbides. Meanwhile, Fig. 15b and d shows that the size of the carbides was approximately 6 µm and that the morphology was spherical. This suggests that the carbides were M_6C instead of $M_{12}C$. Thus, one can conclude that cracks first formed at the interface of the M_6C carbide during the tensile deformation process. The precipitation and growth of $M_{12}C$ at the grain boundary did not deteriorate the tensile properties of the welded joint. The fracture mechanism of the as-welded and thermally exposed joints was mainly the ductile fracture of the microporous aggregate.

As shown by the above results, the fracture position and mechanism of the welded joint were unaffected by changes in the quantity and size of the precipitated phase. Moreover, based on our previous study [25], the BM is weaker than the FZ and HAZ. Although the quantity and size of the precipitated phase in the welded joints increased with the thermal-exposure time, as shown in Figs. 9 and 13, the degree of precipitation strengthening in each zone of the welded joints was similar. Therefore, the strength distribution in each zone of the welded joints after thermal exposure remained similar to that of the as-welded joint, which resulted in the rupture of the BM.

4 Conclusion

(1) After thermal exposure for 10000 h at 700 °C, the grain sizes of the FZ, HAZ, and BM were approximately 5% larger than those of the as-welded joint.
(2) Fine M_6C precipitated in the interdendritic region of the FZ, which enlarged and spheroidized as thermal exposure progressed. The M_6C-γ eutectic carbide of the FZ decomposed from strip to spheres, and the total amounts of primary and secondary carbides stabilized after thermal exposure for 3000 h.
(3) The fracture location was in the BM and the primary M_6C carbide became the main crack source during the tensile deformation process. The precipitation and evolution of the carbides in the FZ and HAZ did not affect the tensile properties of the joints.

Author Contributions All authors contributed to the study conception and design. Material preparation, data collection and analysis were performed by KY, YZ, XDY, LBZ and ZJL. The first draft of the manuscript was written by KY, and all authors commented on previous versions of the manuscript. All authors read and approved the final manuscript.

Data availability statement The data that support the findings of this study are openly available in Science Data Bank at https://cstr.cn/31253.11.sciencedb.j00186.00189 and https://doi.org/10.57760/sciencedb.j00186.00189.

Declaration

Conflict of interest The authors declare that they have no Conflict of interest.

References

1. J. Uhlíř, Chemistry and technology of molten salt reactors-history and perspectives. J. Nucl. Mater. **360**, 6–11 (2007). https://doi.org/10.1016/j.jnucmat.2006.08.008

2. D. LeBlanc, Molten salt reactors: a new beginning for an old idea. Nucl. Eng. Des. **240**, 1644–1656 (2010). https://doi.org/10.1016/j.nucengdes.2009.12.033
3. J. Serp, M. Allibert, O. Beneš et al., The molten salt reactor (MSR) in generation IV: overviewand perspectives. Biol. Sci. **77**, 308–319 (2014). https://doi.org/10.1016/j.pnucene.2014.02.014
4. J.J. Li, Y.L. Qian, J.L. Yin et al., Large eddy simulation of unsteady flow in gas-liquid separator applied in thorium molten salt reactor. Nucl. Sci. Tech. **29**, 62 (2018). https://doi.org/10.1007/s41365-018-0411-3
5. R.M. Ji, Y. Dai, G.F. Zhu et al., Evaluation of the fraction of delayed photoneutrons for TMSR-SF1. Nucl. Sci. Tech. **28**, 135 (2017). https://doi.org/10.10071s41365-017-0285-9
6. L.Y. He, S.P. Xia, X.M. Zhou et al., Th-U cycle performance analysis based on molten chloride salt and molten fluoride salt fast reactors. Nucl. Sci. Tech. **31**, 83 (2020). https://doi.org/10.1007/s41365-020-00790-x
7. I.M. Neklyudov, O.M. Morozov, V.G. Kulish et al., The effects of helium on hydrogen isotope retention in Hastelloy-N. J. Nucl. Mater. **417**, 1158–1161 (2011). https://doi.org/10.1016/j.jnucmat.2010.12.214
8. A.J. Gordon, K.L. Walton, T.K. Ghosh et al., Hemispherical total emissivity of Hastelloy N with different surface conditions. J. Nucl. Mater. **426**, 85–95 (2012). https://doi.org/10.1016/j.jnucmat.2012.03.026
9. H.L. Zhu, R. Holmes, T. Hanley et al., High-temperature corrosion of helium ion-irradiated Ni-based alloy in fluoride molten salt. Corros. Sci. **91**, 1–6 (2015). https://doi.org/10.1016/j.corsci.2014.11.013
10. X.Y. Wang, X. Wang, X.C. Zhang et al., The creep damage characterization of the UNS N10003 alloy was based on a numerical simulation using the Norton creep law and the Kachanov-Rabotnov creep damage model. Nucl. Sci. Tech. **30**, 65 (2019). https://doi.org/10.1007/s41365-019-0586-2
11. B. Zhou, X.H. Yu, Y. Zou et al., Study on dynamic characteristics of fission products in 2 MW molten salt reactor. Nucl. Sci. Tech. **31**, 17 (2020). https://doi.org/10.1007/s41365-020-0730-z
12. K. Wang, L. Jiang, X.X. Ye et al., Absorption effect of pure nickel on the corrosion behaviors of the GH3535 alloy in tellurium vapor. Nucl. Sci. Tech. **32**, 140 (2021). https://doi.org/10.1007/s41365-021-00976-x
13. T. Cui, J.J. Wang, R.G. Guan et al., Microstructures evolution of a Ni-Base Superalloy after long-term aging at 750°C. J. Iron Steel Res. Int. **14**, 40–44 (2007). https://doi.org/10.1016/S1006-706X(08)60049-7
14. Y.M. Li, R.M. Zhu, H.J. Liu et al., Evolution of precipitated phase in GH625 alloy during long term aging. Heat Treatment Metals **42**, 94–99 (2017). https://doi.org/10.13251/j.issn.0254-6051.2017.09.021
15. F.F. Han, B.M. Zhou, H.F. Huang et al., Effect of long-term thermal exposure on the hot ductility behavior of GH3535 alloy. Mater. Sci. Eng. A. **673**, 299–306 (2016). https://doi.org/10.1016/j.msea.2016.07.034
16. T. Liu, J.S. Dong, L. Wang et al., Effect of long-term thermal exposure on microstructure and stress rupture properties of GH3535 superalloy. J. Mater. Sci. Technol. **31**, 269–279 (2015). https://doi.org/10.1016/j.jmst.2014.07.021
17. J.M. Leitnaker, G.A. Potter, D.J. Bradley et al., The composition of eta carbide in hastelloy N after aging 10,000 h at 815°C. Metall. Trans. A. **9**, 397–400 (1978). https://doi.org/10.2172/5441556
18. S.J. Chen, X.X. Ye, K. Yu et al., Microstructure and mechanical properties of UNS N10003 alloy welded joints. Mater. Sci. Eng. A. **682**, 168–177 (2017). https://doi.org/10.1016/j.msea.2016.10.122
19. J.G. Yang, Y.M. He, C.J. Qin et al., Microstructure evolution in a Ni-Mo-Cr superalloy subjected to simulated heat-affected zone thermal cycle with high peak temperature. Mater. Des. **86**, 230–236 (2015). https://doi.org/10.1016/j.matdes.2015.07.085
20. Y.M. He, J.G. Yang, C.J. Qin et al., Characterization of the Ni-Mo-Cr superalloy subjected to simulated heat-affected zone thermal cycle treatment. J. Alloy. Compd. **643**, 7–16 (2015). https://doi.org/10.1016/j.jallcom.2015.04.126
21. D. Bhattacharyya, J. Davis, M. Drew et al., Characterization of complex carbide-silicide precipitates in a Ni-Cr-Mo-Fe-Si alloy modified by welding. Mater. Charact. **105**, 118–128 (2015). https://doi.org/10.1016/j.matchar.2015.05.001
22. S. Chen, L. Zhao, J. Wang et al., Microstructure evolution and mechanical properties of simulated HAZ in a Ni-17Mo-7Cr superalloy: effects of the welding thermal cycles. J. Mater. Sci. **55**, 13372–13388 (2020). https://doi.org/10.1007/s10853-020-04927-6
23. W.X. Wang, C.W. Li, L. Jiang et al., Evolution of carbide precipitates in Hastelloy N joints during welding and post weld heat treatment. Mater. Charact. **135**, 311–316 (2018). https://doi.org/10.1016/j.matchar.2017.11.045
24. K. Yu, Z.G. Jiang, B. Leng et al., Effects of post-weld heat treatment on microstructure and mechanical properties of laser welds in GH3535 superalloy. Opt. Laser Technol. **81**, 18–25 (2016). https://doi.org/10.1016/j.optlastec.2016.01.029
25. K. Yu, Z.G. Jiang, C.W. Li et al., Microstructure and mechanical properties of fiber laser welded GH3535 superalloy. J. Mater. Sci. Technol. **33**, 1289–1299 (2017). https://doi.org/10.1016/j.jmst.2016.11.026
26. M.L. Zhu, D.Q. Wang, F.Z. Xuan, Effect of long-term aging on microstructure and local behavior in the heat-affected zone of a Ni-Cr-Mo-V steel welded joint. Mater. Charact. **87**, 45–61 (2014). https://doi.org/10.1016/j.matchar.2013.10.026
27. K. Yu, X.W. Shi, Z.G. Jiang et al., Effects of solution treatment on grain coarsening and hardness of laser welds in UNS N10003 alloy contained different carbon content. J. Mater. Sci. Technol. **35**, 1719–1726 (2019). https://doi.org/10.1016/j.jmst.2019.03.016
28. L. Jiang, W.Z. Zhang, Z.F. Xu et al., M_2C and M_6C carbide precipitation in Ni-Mo-Cr based superalloys containing silicon. Mater. Des. **112**, 300–308 (2016). https://doi.org/10.1016/j.matdes.2016.09.075
29. E. Orowan, Fracture and strength of solid metals. Rep. Prog. Phys. **12**(1), 185–232 (1949). https://doi.org/10.1088/0034-4885/12/1/309
30. K. Han, H.Q. Wang, L. Shen et al., Analysis of cracks in the electron beam welded joint of K465 nickel-base superalloy. Vaccum **157**, 21–30 (2018). https://doi.org/10.1016/j.vacuum.2018.08.011
31. Y.P. Mei, Y.C. Liu, C.X. Liu et al., Effect of base metal and welding speed on fusion zone microstructure and HAZ hot-cracking of electron-beam welded Inconel 718. Mater. Des. **89**, 964–977 (2016). https://doi.org/10.1016/j.matdes.2015.10.082